

Characterization of Lung Tissues using Liquid-Crystal Tunable Filter and Hyperspectral Imaging System

Jong-Ha Lee and Chang-Hee Won

Abstract—Hyperspectral imaging system has been developed to characterize lung tissue for detecting emphysematous tissues in lung volume reduction surgery. The system consists of a charge-coupled device and liquid crystal tunable filter, which is continuously tunable in the near-infrared spectral range of 650 – 1100 nm with a mean bandwidth of 5 nm. Using hyperspectral data, the spectral signature of healthy lung tissue and simulated smokers lung tissue is obtained and compared. The data show the peak absorption intensity at four different wavelengths (760, 805, 915, and 970 nm). However, the reflectance intensity of simulated smoker’s lung tissue over all spectral range is considerably higher than the normal lung tissue. The differences provide the basis for the detection and characterization of emphysema from healthy lung tissue.

I. INTRODUCTION

Emphysema is an obstructive lung disease affecting millions of people, especially smokers around the world. It is characterized by a loss of elasticity, which results in an early airway closure during exhalation. The normal anatomy of the lung is altered in such a way that gas exchange becomes poor. According to the National Center for Health Statistics, the number of non-institutionalized adults who have ever been diagnosed with emphysema was 4.1 million in 2006 [1]. In the United States, emphysema also contributes to more than 100,000 deaths each year, and costs more than 2.5 billion dollars in annual health care expenses [2]. National emphysema treatment trial shows that lung volume reduction surgery (LVRS) improves the quality of life by improving the exercise capacity [3]. The same study also concludes that for patients with both predominantly upper-lobe emphysema and low base-line exercise capacity, LVRS reduces mortality. A more recent study shows the improvements in pulmonary function and exercise ability after LVRS [4], [5]. There are also studies that LVRS improves neuropsychological function and sleep quality [6]. Thus, LVRS benefits the patients with severe emphysema, and the improvements of LVRS equipments and procedure should also benefit the patients. Currently, surgeons perform LVRS largely depend on the “touch sensation” of the tissues and experiences. There is no good method to quantify and display the severity of emphysema. This is an important issue in training young surgeons. Consequently, there is a strong need to quantify

and characterize the lung tissue and relay the information to the surgeons.

The authors propose to improve the quality of surgery by devising the portable hyperspectral imaging system (HIS) to characterize lung tissue in the operating room. HIS is a novel method to generate spectral characteristics of region of interest (ROI) based on the chemical composition. This information is interpreted as the spectral signature of the tissues. HIS has several advantages compare to other modalities such as CT and MRI for detecting emphysema. The system obtains hyperspectral image data during the surgery in near real time, it can compensate for tissue deformation. NIR light penetrates biological tissues without radiation exposure. In addition, it is portable and cost effective compared to other modalities such as MRI. We hypothesize that this system will improve the precision and quality of LVRS. consequently improving the morbidity and mortality of patients with severe emphysema. Furthermore, HIS can be used to train new surgeons in determining the line of resection in LVRS.

In this paper, we developed a portable HIS and characterized lung tissue conditions using NIR wavelengths. HIS is integrated with charge-coupled device (CCD) and liquid crystal tunable filter (LCTF) to capture the spectral information. Human tissues have optical signatures that reflect their chemical compositions. The primary compositions of human tissue are oxyhemoglobin (HbO_2) and deoxyhemoglobin (Hb). Hb further breaks down into melanin, lipids and water (oxygenation, O_2). Total hemoglobin (HbT) indicates the combined quantities of HbO_2 and Hb . In near infrared (NIR) region, HbO_2 and Hb are major absorber of spectrum [7]. Because many diseases such as emphysema have specific effects on tissue oxygenation and blood supply, HbT concentrations are major indicators of viability and tissue health. We focus on the NIR region, particularly the short wavelength NIR (SNIR) from 650 nm to 1100 nm. Since SNIR covers visible light from 650 nm to 700 nm of red color, the color difference between normal and emphysematous tissues is also determined. By comparing the acquired absorption spectrum in the SNIR region, the type, location and relative concentration of chemical composition of the tissues can be determined.

Normal pig’s lung phantom and smoker’s lung phantom are used in the experiments. The spectral signature of three different region of interest (ROI) on each phantom’s surface are obtained and characterized. The experimental study demonstrates the system capability to characterize the lung tissue, and a method to discriminate it from the unhealthy lung tissues.

This work was supported by the Provost office and the Office of the Senior Vice President for Research and Strategic Initiatives at Temple University
Jong-Ha Lee is with the Department of Electrical and Computer Engineering, Temple University, Philadelphia, PA 19122, USA
jong@temple.edu

Chang-Hee Won is with Faculty of Electrical and Computer Engineering, Temple University, Philadelphia, PA 19122, USA
cwon@temple.edu

II. EXPERIMENTAL SETUP

A. Hyperspectral Imaging System Description

The portable hyperspectral tunable imaging system consists of 1.4 megapixel, 12 bit digital imager (Qimaging Inc., Surrey, British Columbia), Liquid Crystal Tunable Filter (LCTF, Cambridge Research & Instrumentation Inc., Woburn, Massachusetts), and LCTF controller. The digital imager is a mono-cooled charge coupled device (CCD) with $6.45 \mu\text{m}$ (V) \times $6.45 \mu\text{m}$ (H) individual pixel size. LCTF is placed in front of the digital imager and filter bands in the short wavelength NIR range from 650 nm to 1100 nm. The filter is set to 5 nm full width at half maximum (FWHM). The FWHM is measured as the spectral separation between two points where the filter's transmission attains 50 % of the peak value. The LCTF controller synchronizes between digital imager and LCTF. It also varies the programmed sequential bands of filter. The tuning speed of the filter is between 50 ms to 150 ms.

All images are captured with 91 bands with center wavelengths separated by 5 nm. Data produced by HIS can be represented by a 3-D cube of image $I(x, y, \lambda_k)$, where (x, y) indicates the spatial coordinate of a pixel, $x=1,2,\dots,1392$, $y=1,2,\dots,1090$, and λ_k denotes the wavelength of the k^{th} spectral band. Each value of $I(x, y, \lambda_k)$ is quantified by a gray scale level and has a minimum value of 0 and has a maximum value of $2^{16} = 4096$. Individual 3-D cube of images are stored in a 12 bit binary format along a header file containing image parameter information. The data size of one image is approximately 1392 pixels \times 1040 pixels \times 91 bands \times 12 bits = 197 megabytes. LCTF tuning, image acquisition, and storage are managed by a software compile by C++. A high-end laptop computer (Apple MacBook Pro 2.53 GHz, Cupertino, CA) manages the instrument control, spectral image acquisition and synchronization. Image visualization is performed using ENVI software (Ver. 4.5, ITT Visual information solutions, Boulder, CO) environment. Fig. 1 shows the proposed HIS system setup.

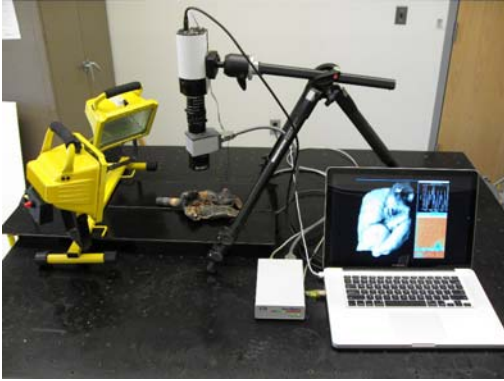


Fig. 1. Schematic diagram of the portable hyperspectral imaging system. The connection consists of three parts. From computer to LCTF controller, 1394 cable is connected. From LCTF controller to camera, parallel port cable is used. From camera to computer, USB cable is connected. The synchronization of this connection is handled in the computer.

Total scanning time of LCTF is about 23 seconds including data transferring to computer and image rendering to screen for surgeon. To cover SNIR range, dual 500 watts white quartz tungsten halogen lamps with the wavelength ranging from 360 nm to 2500 nm is used. Fig. 2 represents the tunable filter transmission characteristics under dual halogen light excitation.

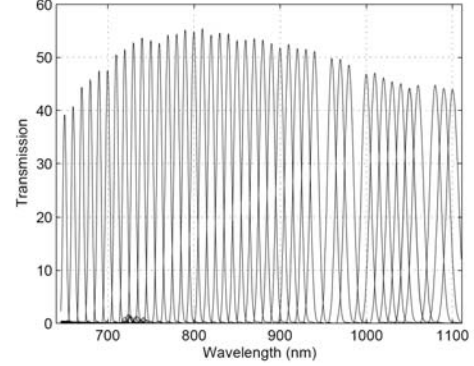


Fig. 2. Transmission characteristic of tunable filter at SNIR 650 nm – 1100 nm. The transmission data indicates the calibrated condition of tunable filter.

B. Optics Calibration

Image intensity data from digital imager contains unknown system offsets and gains, thus it may vary over time. Consequently, optics calibration steps are necessary. According to [8], image intensity at spatial coordinate (x, y) at λ_k band can be modeled as

$$I(x, y, \lambda_k) = L(x, y, \lambda_k)S(x, y, \lambda_k)R(x, y, \lambda_k) + O(x, y, \lambda_k) \quad (1)$$

where $k=1,2,\dots,91$. $L(x, y, \lambda_k)$ refers to the illumination, $S(x, y, \lambda_k)$ refers to the system spectral response, $R(x, y, \lambda_k)$ refers to the reflectance of the viewed surface, and $O(x, y, \lambda_k)$ is the offset due to the stray light. To compensate unknown system offsets and gains, Spectralon diffuse reflectance standards SRS-99 for an approximately 99 % reflectance and SRS-02 for an approximately 2 % reflectance (Labsphere, Sutton, NH) are used. These standards used in the optics calibration are directly traceable to the US National Institute of Standards and Technology (NIST). For the image intensity of SRS-99 spectralon, we have

$$I_{99}(x, y, \lambda_k) = L(x, y, \lambda_k)S(x, y, \lambda_k)R_{99}(x, y, \lambda_k) + O(x, y, \lambda_k) \quad (2)$$

And for the image intensity of SRS-02 spectralon, we have

$$I_{02}(x, y, \lambda_k) = L(x, y, \lambda_k)S(x, y, \lambda_k)R_{02}(x, y, \lambda_k) + O(x, y, \lambda_k) \quad (3)$$

where $R_{99}(\lambda_k)$ and $R_{02}(\lambda_k)$ are reflectance functions for these two images and theoretically independent of (x, y) because the spectralon surface has the same reflectance property for all image pixels. By using the equations for $I_{99}(\lambda_k)$ and $I_{02}(\lambda_k)$, we derive

$$L(x, y, \lambda_k) = \frac{I_{02}(x, y, \lambda_k) - I_{99}(x, y, \lambda_k)}{R_{02}(\lambda_k) - R_{99}(\lambda_k)} \quad (4)$$

During the calibration, 20 different spectralon images are obtained and averaged to estimate $I_{99}(\lambda_k)$ and $I_{02}(\lambda_k)$. With this estimates, the final reflectance is given as below:

$$R(x, y, \lambda_k) = \frac{(I(x, y, \lambda_k) - I_{99}(x, y, \lambda_k))R_{02}(\lambda_k)}{I_{02}(x, y, \lambda_k) - I_{99}(x, y, \lambda_k)} + \frac{(I_{02}(x, y, \lambda_k) - I(x, y, \lambda_k))R_{99}(\lambda_k)}{I_{02}(x, y, \lambda_k) - I_{99}(x, y, \lambda_k)} \quad (5)$$

Finally, the reflectance $R(x, y, \lambda_k)$ of samples are converted to the apparent absorbance, $A(x, y, \lambda_k)$, defines as the logarithm of the ratio between reflectance of the sample $R(x, y, \lambda_k)$, and the reflectance of certified 99 % standard, measured at the wavelength λ_k and the spatial coordinates (x, y) [9]

$$A(x, y, \lambda_k) = \log \frac{R_{SRS-99}(\lambda_k)}{R(x, y, \lambda_k)} \quad (6)$$

If ROI is more than one pixel, the apparent absorbance vector of each ROI is averaging over $M + N$ pixels according to

$$A_{ave}(x, y, \lambda_k) = \frac{1}{M + N} \sum_{j=1}^N \sum_{i=1}^M A(x, y, \lambda_k) \quad (7)$$

This optics calibration step is performed in the beginning of every experiments.

C. SNIR Depth Penetration

The light in NIR spectrum is known to penetrate into tissue farther than other spectrum due to tissue's low absorption and optimal image processing techniques [10]. Formally, the NIR penetration depth is defined as

$$\delta = \frac{1}{\sqrt{3\mu_a(\mu_a + \mu'_s)}} \approx \frac{1}{\sqrt{3\mu_a\mu'_s}} \quad (8)$$

where μ_a is the absorption coefficient and μ'_s is the reduced scattering coefficient of the tissue, respectively. For a typical healthy lung, under the illumination power of 10 mW, $\mu_a=11.3 \text{ mm}^{-1}$ and $\mu'_s=72.3 \text{ mm}^{-1}$ at 630 nm band (NIR). For an unhealthy lung, $\mu_a=49.2 \text{ mm}^{-1}$ and $\mu'_s=12.1 \text{ mm}^{-1}$ at the same band [11]. This leads to a light penetration depth of 3.42 mm for a healthy lung tissue and 2.81 mm for an unhealthy lung (lung-tumor) tissue at 630 nm band. The degree of penetration depth varies depending on the spectral band and the light source. Because NIR light penetrates into biological tissue, the spectral signature of composition under the surface can be obtained.

III. HYPERSPECTRAL DATA ACQUISITION AND ANALYSIS

In this section, we discuss the results of our experimental observations. The aim of these experiments is to demonstrate the potential of HIS for the lung tissue characterization and discriminate it from unhealthy lung tissue. For a lung tissue characteristic experiment, a pig's lung is used. Totally 91 spectral band images, each image of 1392×1040 pixels in size are obtained within 23 seconds. Dual 500 W quartz tungsten halogen lamps are used for illumination. Samples

are kept in iced bags to minimize dehydration and then placed in a tray without ice while hyperspectral images are acquired. To demonstrate the capability of HIS to produce spectral contrast between different regions on a lung surface, three ROIs are initially identified based on the visual sense and recorded as left lung, right lung, and cardiac notch. The ROI is a rectangular shape containing 100×100 pixels each. The lung phantom with three ROIs is shown in Fig. 3.

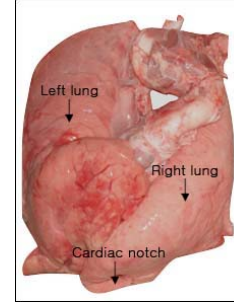


Fig. 3. Lung phantom with three different ROIs on the left lung, right lung, and cardiac notch.

Fig. 4 shows the measured spectrum of ROIs. The graph is drawn based on the average of 100×100 pixels apparent absorbance $A(x, y, \lambda_k)$. The range of $A(x, y, \lambda_k)$ is from 0 to 8.307. Because of Hb and HbO_2 blood vessels near the surface of the lung, a spectrum have peaks of Hb and HbO_2 at 760 nm and 805 nm, respectively. The spectrum also indicates significant lipids and water absorption at 915 nm and 970 nm. We expect that this is due to the uncalibrated light source and sample condition. In addition to four peaks, the spectrum has a peak value of 1005 nm, 1035 nm, and 1070 nm due to the mixture of constituents in the lung.

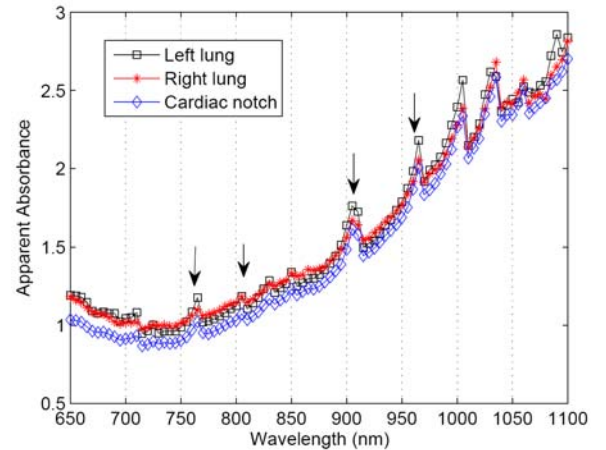


Fig. 4. Reconstructed apparent absorbance spectrum of ROIs from healthy left lung, right lung, and cardiac notch. Spectrum contains an absorption peak at 760 nm, characteristic of Hb followed 805 nm peak typical of HbO_2 , with lipids at 915 nm and 970 nm for water. The peak beyond 970 nm is for a molecular mixture consistent with known constituents contained within lung.

Based on the healthy lung tissue characteristic, we can compare it from unhealthy lung tissue. For this experiment,

the simulated smoker's lung is used. We hypothesize that emphysematous lung have reduced absorption. Similar to the previous experiment, 91 spectral band images with each image of 1392×1040 pixels in size are obtained. Three different regions are determined by 100×100 pixels and 10,000 apparent absorption spectrum of each pixel are calculated and averaged. Statistical comparison is done using raw reflectance $R(x, y, \lambda_k)$. Fig. 5. represents the mean and standard deviation of reflectance of three ROIs on healthy lung and simulated smoker's lung each. The range of $R(x, y, \lambda_k)$ is from 0 to $2^{16} = 4096$. We notice that two types of tissues have similar spectrum patterns, but the reflectance of the smoker's lung is significantly higher than the healthy lung. This is because the spectral signature is highly dependent on the composition of tissues. Emphysema affects the tissue oxygenation and blood supply. The damaged tissue contains less HbT and water which absorbs NIR light [12]. More HbT and water implies smaller reflectance. Consequently, less HbT and water implies higher reflectance. From the reflectance profile, we quantify the severity of emphysema at four obvious peak wavelength bands that we found from previous experiments. For example, at 760 nm, the reflectance range 324 – 447 would be a healthy lung tissue. Similarly the range 254 – 355 at 805 nm, 109 – 157 at 915 nm, and 45 – 65 at 970 nm defines the healthy lung tissue. Farther away from this range will be considered as an unhealthy. Therefore, the range 1300 – 2139 at 760 nm, 945 – 1529 at 805 nm, 506 – 801 at 915 nm, and 156 – 272 at 970 nm that corresponds to the simulated smoker's lung would be considered as unhealthy. From this difference of spectral signature, we can distinguish between healthy and unhealthy lung tissues.

During the experiment, 500W white light source was used and it increased the tissue temperature. For the clinical use, this light source will be replaced by the LED light source with similar brightness. The imaging time during the open organ surgery is also important issue. Since we found four specific wavelengths that characterize the tissues, HIS will use these four wavelengths, which will significantly reduce the imaging time.

IV. CONCLUSIONS

In this paper, we describe the development of a hyperspectral imaging system that combines several advances in photonics technologies, including CCD and LCTF. The LCTF is tunable over the spectral range of 650 – 1100 nm. The capability of the system has been proven through phantom lung studies. Throughout the experiment, we find that HIS imaging technology can provide a method to measure total hemoglobin concentration and oxygenation saturation differences between normal lung and unhealthy lung tissue. Thus the apparent absorption and reflectance differences between normal tissues and simulated emphysematous tissues have been readily seen using HIS. Consequently, the system will be an efficient tool for a lung volume reduction surgery.

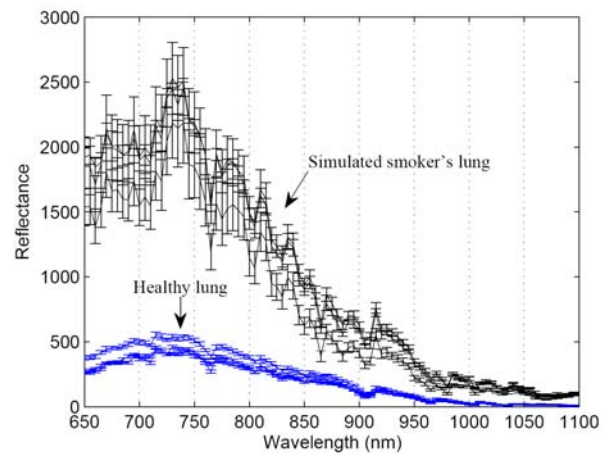


Fig. 5. Comparison of reflectance of three ROIs of healthy lung and simulated smokers lung each. Two types of tissue have similar wavelength pattern. However the reflectance intensity of simulated smokers lung is much higher than healthy lung.

REFERENCES

- [1] National Center for Health Statistics, U.S. Department of Health and Human Services, Center for Disease Control and Prevention, Available: <http://www.cdc.gov/nchs/fastats/emphysema.htm>
- [2] National Emphysema Treatment Trial Research Group, "A randomized trial comparing lung-volume-reduction surgery with medical therapy for severe emphysema," *The New England Journal of Medicine*, vol. 384, num. 11, pp. 2059-2073, March 2003.
- [3] National Emphysema Treatment Trial Research Group, "Safety and efficacy of median sternotomy versus video-assisted thoracic surgery for lung volume reduction surgery," *The Journal of Thoracic and Cardiovascular Surgery*, vol. 127, num. 5, pp. 1350-1360, May 2004.
- [4] P. Lawson, "Lung volume reduction surgery for severe emphysema increases exercise capacity but does not affect mortality," *An International Journal of Respiratory Medicine*, vol. 58, num. 8, pp. 720, August 2003.
- [5] J.D. Miller, R.A. Malthaner, C.H. Goldsmith, R. Goeree, D. Higgins, P.G. Cox, L. Tan, and J.D. Road, "A Randomized Clinical Trial of Lung Volume Reduction Surgery Versus Best Medical Care for Patients With Advanced Emphysema: A Two-Year Study From Canada," *The Annals of Thoracic Surgery*, vol. 81, pp. 314-321, July 2005.
- [6] E. Kozora, C.F. Emery, M.C. Ellison, F.S. Wamboldt, P.T. Diaz, and B. Make, "Improved Neurobehavioral Functioning in Emphysema Patients Following Lung Volume Reduction Surgery Compared With Medical Therapy," *Chest*, vol. 128, num. 4, pp. 2053-2063, October 2005.
- [7] P. Taroni, A. Pifferi, A. Torricelli, and R. Cubeddu, "Time-Resolved Optical Spectroscopy and Imaging of Breast," *Opto-Electronics Review*, vol. 12, num. 2, pp. 249-253, 2004.
- [8] Z. Pan, G. Healey, M. Prasad, and B. Trombery, "Face Recognition in Hyperspectral Images," *IEEE Transaction on Pattern Analysis and Machine Intelligence*, vol. 25, no. 12, pp. 1552-1560, December 2003.
- [9] K. Zuzak, S. Naik, G. Alexandrakis, D. Hawkins, K. Behbehani, and E. Livingston, "Characterization of a Near Infrared Laparoscopic Hyperspectral Imaging System for Minimally Invasive Surgery," *Analytical Chemistry*, vol. 79, no. 12, pp. 4709-4713, May 2007.
- [10] J. Lammertyn, A. Peris, J. Baerdemaeker, and B. Nicolai, "Light Penetration Properties of NIR Radiation in Fruit with respect to Nondestructive Quality Assessment," *Journal of the Postharvest and Technology*, vol. 18, pp. 121-132, February 2000.
- [11] P. Bargo, "Optical Measurements for Quality Control in Photodynamic Therapy," Ph. D. Dissertation of Electrical and Computer Engineering, Oregon Health & Science University, July 2003.
- [12] R. Xu, D.C. Young, J.J. Mao, and S.P. Pivoski, "A Prospective Pilot Clinical Trial Evaluating the Utility of a Dynamic Near-Infrared Imaging Device for Characterizing Suspicious Breast Lesions," *Breast Cancer Research*, vol. 9, no. 6, December 2007.